Polymer 49 (2008) 2334–2341

Contents lists available at ScienceDirect

Polymer

journal homepage: www.elsevier.com/locate/polymer

Elongation flow-induced morphological change of a diblock copolymer melt of polystyrene and poly(ethylene propylene)

Yong Ku Kwon [a,*], Yoon Soo Ko [a], Masami Okamoto [b,**]

[a] Department of Polymer Science and Engineering, Inha University, 253 Yonghyun-Dong, Nam-Gu, Incheon 402-751, Republic of Korea
[b] Advanced Polymeric Materials Engineering, Graduate School of Engineering, Toyota Technological Institute, Hisakata 2-12-1, Tempaku, Nagoya 468-8511, Japan

ARTICLE INFO

Article history:
Received 21 November 2007
Received in revised form 27 February 2008
Accepted 2 March 2008
Available online 5 March 2008

Keywords:
Elongational flow
Polystyrene-*b*-poly(ethylene propylene)
Small angle X-ray scattering

ABSTRACT

The elongational flow-induced alignment process of a lamellar-forming polystyrene-*b*-poly(ethylene propylene) (SEP) diblock copolymer has been investigated by using elongational flow opto-rheometry (EFOR) and small angle X-ray scattering (SAXS). The lamellar domains of the compression molded SEP were aligned in a preferred direction by roll casting at 200 °C. In the EFOR measurement, the roll-cast film was uniaxially elongated at 180 °C at a Hencky strain rate, $\dot{\epsilon}_o$, of 0.01 s^{-1} in the direction either perpendicular (denotes case I) or parallel (case II) to the direction of the lamellar normal. The apparent retardation, R_{app}, and initial moduli data measured during elongation suggest that either polystyrene (PS) or poly(ethylene propylene) (PEP) domain is preferentially elongated during the early stage of elongation. Transient elongational viscosity, $\eta(\dot{\epsilon}_o; t)$, measured during the case I elongation exhibits a continuous increase up to rupture with the absence of a morphological change. One measured during the case II elongation shows an initial increase up to 20 s, followed by a slight decrease by 80 s prior to a predominant increase before rupture. The SAXS patterns of the elongated samples show that the lamellar domains subjected in the case I elongation persist during elongation without any prominent structural change, whereas those subjected in the case II elongation are highly deformed and rotated by about 90°, displaying a strong strain-induced hardening in the final stage of elongation.

1. Introduction

Nanophase-separated block copolymers exhibit various domain structures at a given temperature, depending on the nature and volume fraction of each block segment in a block copolymer chain [1]. A further aggregation of domains forms a grain structure, usually in a micrometer scale, which is isotropic in a quiescent state. The application of an external field to block copolymers leads to the changes in geometry, size and orientation of the domain and grain structure that influence macroscopic and rheological response of block copolymers during deformation process. The alignment process of domains of block copolymers has been extensively investigated under hydrodynamic flow fields [2–9]. Most of the studies focus on the deformation behavior induced by large strain oscillatory shear that produces the global orientation of domains in a preferred direction. The aligned morphology mainly depends on the experimental variables such as shear rate, as well as processing and thermal history acquired prior to the measurement. Polis and Winey demonstrated the continuous rotation process of the lamellae of a diblock copolymer of polystyrene-*b*-poly(ethylene propylene) under a large amplitude oscillatory shear and explained the formation of kink bands in the sheared lamellae by layer rotation mechanism [3]. A lamellar-forming diblock copolymer of polystyrene-*b*-polyisoprene (SI) system displays either perpendicular (with lamellar normal along the vorticity direction) or parallel (with lamellar normal along the shear gradient direction) alignment depending on the shearing condition [10–12]. For a presheared SI system with intermediate molecular weight, transverse (with lamellar normal along the shear direction) orientation is also found near the glass transition temperature of polystyrene, which may be related to the kink band structure among the perpendicular lamellae during deformation process. Shearing also induces mixed orientations, composed of the parallel, transverse and perpendicular lamellae that appear as nonequilibrium, transient states of deformed morphology.

Elongation of block copolymers has attracted recent research interest due to their interesting morphological responses at large deformation [13–19]. We recently have studied on the elongational flow-induced morphology change of multiphase polymeric systems [20–23] and a series of block copolymer melts [24–26] such as polystyrene-*b*-poly(ethylene butylene)-*b*-polystyrene (SEBS) triblock copolymer and polystyrene-*b*-poly(ethylene butylene)-*b*-polystyrene-*b*-poly(ethylene butylene) (SEBSEB) tetrablock copolymer by

* Corresponding author. Tel.: +82 32 860 7482; fax: +82 32 865 5178.
** Corresponding author.
E-mail addresses: ykkwon@inha.ac.kr (Y.K. Kwon), okamoto@toyota-ti.ac.jp (M. Okamoto).

0032-3861/$ – see front matter © 2008 Elsevier Ltd. All rights reserved.
doi:10.1016/j.polymer.2008.03.002

using elongational flow opto-rheometry (EFOR), small angle X-ray scattering (SAXS) and transmission electron microscopy (TEM). In this series of researches, the samples were subjected to elongational flow field at various temperatures between the glass transition temperature ($T_{g,PS}$) of polystyrene (PS) and their order–disorder transition (ODT) temperatures. For SEBS melt, uniaxial elongation was applied in the direction either parallel (denotes case I) or perpendicular (case II) to the cylinder axis field at temperatures between the $T_{g,PS}$ and the ODT. The data showed that the PS or poly(ethylene butylene) (PEB) domain was preferentially deformed in the early stage of elongation, which displayed different elongational behavior in both elongation experiments. The case I elongation improved the orientation of the cylinders without any prominent morphological change, whereas the case II elongation highly deformed the domain and grain structure of the perpendicularly aligned cylinders to the stretching direction through the fragmentation and realignment processes.

The morphology of the elongated SEBS samples was mainly controlled by elongational conditions such as strain rate and temperature, rather than the orientation of the initial morphology prior to the elongation measurement. During the elongation at high strain rates, the elongated morphology was largely inclined, whereas the cylinders were highly aligned along the elongational direction at slow strain rates. The parallel orientation obtained at slow strain rates during the case II elongation resulted from the deformation of the mechanically soft PEB domain which caused the fragmentation of the domain and grain structure, followed by realignment of the fragmented and deformed domains into the elongation direction. For SEBSEB melt with a spherical morphology, the spheres subjected to the elongational flow field were deformed into the ellipsoids, similar to the lamellar geometry with structural anisotropy. In addition, the interfaces between the domains become irregular due to their deformation under elongation.

In a series of researches on the elongational flow-induced morphology change of multiphase polymeric systems, we carry out the elongation experiment of a lamellar-forming diblock copolymer of polystyrene-*b*-poly(ethylene propylene) (SEP) in the temperature regime of lamellar phase. The elongational behavior of lamellar-forming diblock copolymers has not been studied much, because they do not persist at a high degree of deformation, as compared with the one measured in cylinder or spherical phase, due to the absence of the bridging or continuous phase connected between domains. However, relatively-high molecular weight diblock copolymers in the strong segregation limit display well-defined interfaces between domains and exhibit improved mechanical properties due to the entanglement of component polymer chains in each domain. In the present study, we demonstrate the elongation experiment of a lamellar-forming SEP diblock copolymer with relatively-high molecular weight, in an attempt to provide information on the deformation process of lamellar morphology with the absence of the bridging structure. The initial morphology of the sample is also precisely controlled by roll casting and subjected to elongational flow field in the direction either parallel or perpendicular to the layer normal. The elongation experiment was carried out at a slow Hencky strain rate of 0.01 s^{-1} and 180 °C, in order to visualize the precise dynamic process of the morphological change of the lamellar phase at large deformation. The deformation behavior of the cylinder and lamellar phase with the change of morphological characteristics will be compared.

2. Experimental

2.1. Materials

The lamellar-forming diblock copolymer, SEP, with PS weight fraction of 38% was kindly provided by *Shell Chemical Co*. and used in this study without any further purification. The molecular weight of the polymer was determined by gel permeation chromatography (GPC) using PS elution standards: the weight-average molecular weight, M_w, was 147.5 kg mol^{-1} and the polydispersity index, M_w/M_n, was around 1.12. The ODT of SEP could not be detected up to ~300 °C in our rheological measurement and was expected to be greater than 300 °C. The block sequence of the polymer was estimated to be 56.1–91.5 kg mol^{-1} for the PS and PEP block segment.

2.2. Sample preparation

The compressed films of as-received SEP powder were prepared by molding at 200 °C. The alignment of the lamellar domains prior to elongation measurement was achieved by uniaxial roll casting by counterrotating two rollers at 200 °C for about 10 min. After alignment by roll casting, the layer normal was set to be aligned perpendicular to the rolling direction. These roll-cast films were then subsequently transferred to another hot-press, kept at ambient temperature and pressure without applying load, and cooled by circulating chilled water into the jacket of the hot-press. Specimens for the EFOR measurements with dimensions of 60.0 ± 0.8 (length) $\times$ 6.5 ± 0.4 (width) $\times$ 1.5 ± 0.5 (thickness) mm^3 were prepared by cutting the roll-cast sheet in the direction either parallel (denotes case I) or perpendicular (case II) to the rolling direction. In order to induce the same thermal and processing history on all tested samples, they were cut from the same roll-cast film. The orientation of the lamellar phase of the initial, unelongated samples was monitored by SAXS. During the EFOR measurements, the samples were collected at various elongation stages and quenched into ice water to freeze the elongated morphology. These elongated samples were kept at room temperature prior to SAXS measurement. Whether the relaxation process of the elongated morphology was occurred was confirmed by SAXS measured just after the EFOR measurement.

2.3. SAXS apparatus

The measurements were carried out in a SAXS apparatus consisting of a 6 kW rotating-anode X-ray generator (M06X^{CE}, MAC science Co. Ltd.) with Cu Kα radiation (wavelength $\lambda_{scat} = 0.154$ nm), operated at 50 kV and 24 mA. It includes a Ge monochromator, a point focusing optics, and a vacuum chamber for the incident beam path and scattered beam path and a two-dimensional imaging plate X-ray detector. The distance between the sample and the detector was set as 850 mm. The correction for slit-width smearing was not needed due to the fine cross-section (0.1 mm $\times$ 1 mm) of the primary X-ray beam used in this study. Two-dimensional SAXS patterns of the elongated samples were taken at room temperature and the angular dependence of the SAXS intensity was recorded on the equator and in the azimuthal direction of the observed SAXS pattern and digitally saved for further analysis. One-dimensional SAXS data in the range $0 < q\ (nm^{-1}) \leq 0.4$ and $0.4 < q\ (nm^{-1}) \leq 1.5$ were measured separately with different X-ray exposure times for better visual representation.

2.4. EFOR measurement

The elongational flow opto-rheometer employed in our study was a combination of a Meissner's new elongational rheometer of gas-cushion type commercialized as Rheometrics Melt Elongational Rheometer (RME: *Rheometrics Scientific Co.*) which has been described elsewhere [27]. The EFOR measurements in this study were carried out with a strain rate 0.01 s^{-1} at 180 °C, and another set of data measured at different temperatures and strain rates will be reported in a separate publication. Prior to the

elongation, sample strips were annealed at 180 °C for about 120 s to remove mechanical and thermal history on samples acquired prior to elongation. Estimation of birefringence $\Delta n(\dot{\epsilon}_o; t)$ requires thickness of specimens. Assuming no volume change during elongation, both cross-sectional area and thickness can be estimated from the initial dimensions measured prior to elongation. The specific volume, $\bar{\nu}_{SEP}$, of SEP is assumed to be addition of those of the component homopolymers as shown below:

$$\bar{\nu}_{SEP} = w_{PS}\bar{\nu}_{PS}(T) + w_{PEP}\bar{\nu}_{PEP}(T) \quad (1)$$

where w_{PS} and w_{PEP} are weight fractions, $\bar{\nu}_{PS}(T)$ and $\bar{\nu}_{PEP}(T)$ are the specific volumes of the PS and PEP blocks as a function of temperature, T, which are adopted from the literature data [28] and specific volume data of amorphous low-density polyethylene $[=1.262 + 0.0009 \times (T - 125)]$ [29], respectively. The difference between the intensities of one detector, S_p ($+45°$ inclination to the stretching direction), and the other detector, S_s ($-45°$ inclination to the stretching direction), was offset prior to the EFOR measurement and the time evolution of the birefringence $\Delta n(\dot{\epsilon}_o; t)$ was then measured.

3. Results and discussion

3.1. Stress–strain curve

Fig. 1 shows the plots of the engineering stress, $\sigma'(\dot{\epsilon}_o; t)[= F(\dot{\epsilon}_o; t)/A_o]$ vs. the Hencky strain $\epsilon(t)$ measured during the case I and case II elongations at 180 °C with a strain rate of 0.01 s^{-1}. Measurements were repeated at least three times for each experiment to achieve statistically significant averages. In this figure, we found the higher elongation at break and smaller initial modulus for the case II elongation, whereas it was ruptured shortly in the case I elongation with the greater initial modulus. In addition, the maximum yield stress and strain for the case I elongation were greater than those measured during the case II elongation. The different elongational behavior of the case I and case II elongations arises due to the different geometrical arrangement of the PS and PEP domains to the stretching direction. The elongation of the case I sample, composed of the parallel array of the PS and PEP domain, caused the preferential elongation of the mechanically rigid PS lamellae, showing the higher initial modulus and early rupture. In the case of the case II melt, the alternating arrangement of the PS and PEP domains to the stretching direction led to the preferential elongation of the PEP domains which exhibited the lower initial modulus and the maximum yield stress due to the preferential elongation of the matrix PEP blocks. The lower stress value for the case II melt was due to the alternate arrangement of the PS and PEP domains to the stretching direction. The elongation of the case II melt, comparable to the one from the case I melt, was due to the entanglement of molecules in each domain with a relatively-high molecular weight. The decreases in modulus and yield strain or stress observed in the case I and case II elongations of the SEP melt, as compared with those measured for the SEBS melt, were due to the absence of the bridging conformation for the SEP diblock copolymer.

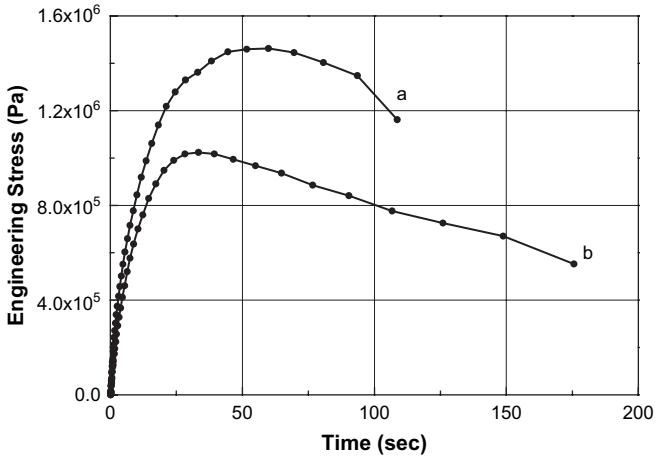

Fig. 1. Engineering stress and strain curves of the SEP samples subjected in the (a) case I and (b) case II elongations.

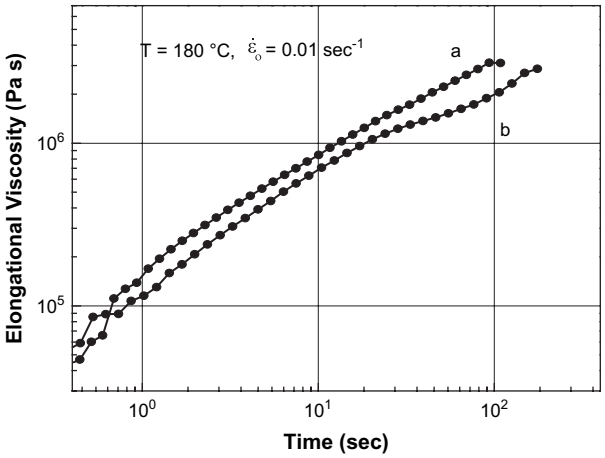

Fig. 2. Plots of elongational viscosity vs. time at 180 °C and with a strain rate of 0.01 s^{-1}: (a) case I and (b) case II elongations.

3.2. Elongational viscosity

The elongational viscosities, $\eta_E(\dot{\epsilon}_o; t)$s, of the case I and case II samples were measured during elongation with a strain rate of 0.01 s^{-1} at 180 °C. Fig. 2(a) shows that the $\eta_E(\dot{\epsilon}_o; t)$ plot of the case I sample increased continuously with time up to its rupture. The initial elongation of the case I sample caused the further alignment of the PS and PEB domains of the roll-cast sample, which led to a continuous increase of the $\eta_E(\dot{\epsilon}_o; t)$ prior to its rupture. The continuous elongation beyond this point caused the rupture of the specimen that reduced the viscosity of the case I melt.

Fig. 2(b) shows the $\eta_E(\dot{\epsilon}_o; t)$ plot of the case II sample, displaying a continuous increase with elongation time until 30 s, but followed by a slight decrease of its increase rate until 100 s where the strain-induced hardening behavior started. Due to the alternate arrangement of the PS and PEB domains to the stretching direction, the initial increase of the $\eta_E(\dot{\epsilon}_o; t)$ of the case II sample resulted from the preferential elongation the soft PEP domain and caused the realignment of the PS and PEP domains to the stretching direction. The slight decrease in the range $30 \leq t\,(s) \leq 100$ was related to the rotation and realignment of the lamellar domains along the elongation direction. In the final stage of elongation, the $\eta_E(\dot{\epsilon}_o; t)$ displayed an increase before rupture, indicative of strain-induced hardening behavior. Both $\eta_E(\dot{\epsilon}_o; t)$ data shown in Fig. 2(a) and (b) did not show any solid plateau region, where $\eta_E(\dot{\epsilon}_o; t)$ was independent of $\dot{\epsilon}_o$, revealing that the steady state of the $\eta_E(\dot{\epsilon}_o; t)$s was almost absent in both cases. The data observed in the beginning of elongation were scattered mostly due to the geometrical distortion of the sample during preannealing prior to the measurements.

3.3. SAXS results

Fig. 3(a) through (e) shows a series of SAXS patterns of the unelongated and elongated case I samples, measured at (a) 0 s

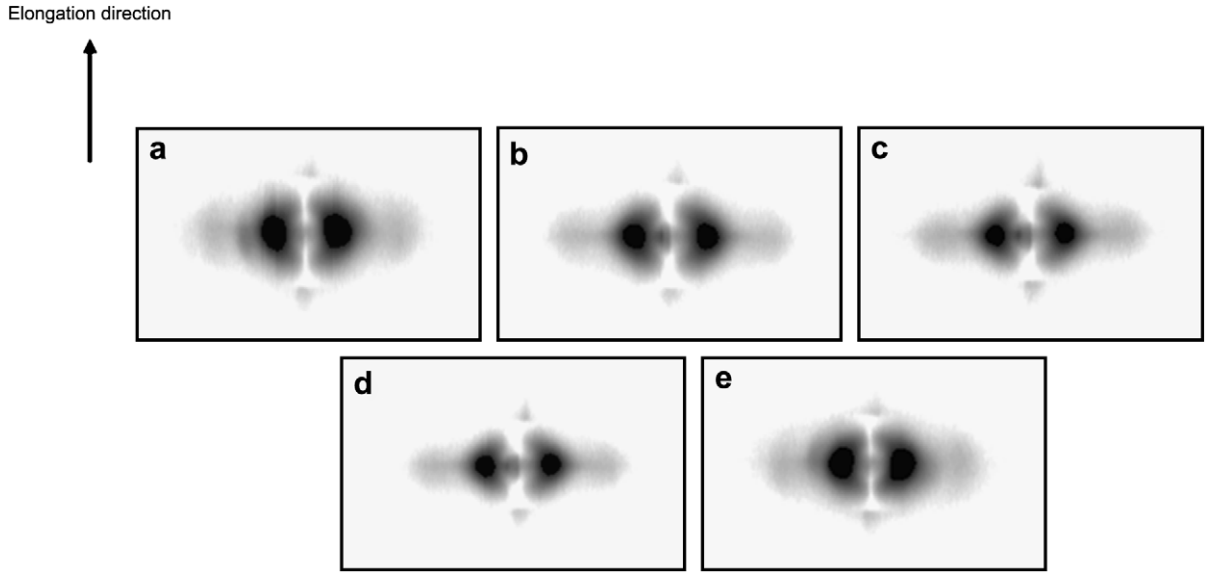

Fig. 3. Two-dimensional SAXS patterns of the unelongated and elongated samples collected during the case I elongation at (a) 0 s (unelongated), (b) 18 s ($\epsilon = 0.18$, $\lambda = 1.20$), (c) 77 s ($\epsilon = 0.77$, $\lambda = 2.16$), (d) 90 s ($\epsilon = 0.90$, $\lambda = 2.46$), and (e) 110 s ($\epsilon = 1.10$, $\lambda = 3.00$).

(unelongated), (b) 18 s ($\epsilon = 0.18$, $\lambda = 1.20$), (c) 77 s ($\epsilon = 0.77$, $\lambda = 2.16$), (d) 90 s ($\epsilon = 0.90$, $\lambda = 2.46$), and (e) 110 s ($\epsilon = 1.10$, $\lambda = 3.00$) during elongation. The corresponding one-dimensional equatorial SAXS intensities $I(q)$ in the 2θ direction vs. the scattering vector, q [$=(4\pi/\lambda_{scat})\sin\theta$, where 2θ is the scattering angle], are also shown in Fig. 4(a) through (e). Each scan has been multiplied by a factor of 10^3 to avoid overlapping between data. The peak in Fig. 4(a) through (e) showed the *100* peak of the lamellar phase, located on the equator. The existence of the equatorial peaks revealed that the alignment of the lamellar normal, which was initially aligned perpendicular to the elongation direction, was maintained during elongation up to rupture. In Fig. 4, we observed an intense *100* peak near $q \sim 0.12\ \mathrm{nm}^{-1}$ with additional weak higher order *200* and *300* peaks in the range $0.2 < q\ (\mathrm{nm}^{-1}) \leq 1.0$. They were approximately in the ratio 1:2:3, indicating the existence of a layer structure before and during elongation. The broadness and weakness of the higher order peak intensities were mostly due to the increased structural distortion of the elongated samples acquired during deformation, as well as the lack of annealing procedure of initial samples prior to measurement. The positions of the intense *100* peak at various stretching ratios determine the average repeat period of the lamellar domain, the same as its average *d*-spacing. In Fig. 5, the *d*-spacing of the *100* peak showed a gradual decrease up to its rupture, due to the improved structural ordering, mainly driven by the further orientation of the lamellar phase along the stretching direction. The characteristic feature shown in Fig. 3(a) through (e) was almost similar, indicating that the morphology of the case I samples was almost maintained during elongation.

Fig. 6(a) through (h) shows the SAXS data of the unelongated and elongated case II samples collected at (a) 0 s (unelongated), (b) 20 s ($\epsilon = 0.2$, $\lambda = 1.2$), (c) 40 s ($\epsilon = 0.4$, $\lambda = 1.5$), (d) 60 s ($\epsilon = 0.6$, $\lambda = 1.8$), (e) 70 s ($\epsilon = 0.7$, $\lambda = 2.0$), (f) 80 s ($\epsilon = 0.8$, $\lambda = 2.2$), (g) 100 s ($\epsilon = 1.0$, $\lambda = 2.7$), and (h) 180 s ($\epsilon = 1.8$, $\lambda = 6.1$). Because the Bragg's peaks from the unelongated or slightly-elongated samples [Fig. 6(a) through (c)] were located on the meridian, the long edge of the rectangular-shaped beam stopper was set perpendicularly to the elongation direction. The corresponding one-dimensional SAXS intensities $I(q)$, scanned through the *100* peak, vs. the scattering vector, q, are also shown in Fig. 7(a) through (i). For the unelongated roll-cast sample, shown in Fig. 7(a), the intense, but broad *100* peak was found on the meridian, confirming that the orientation of the

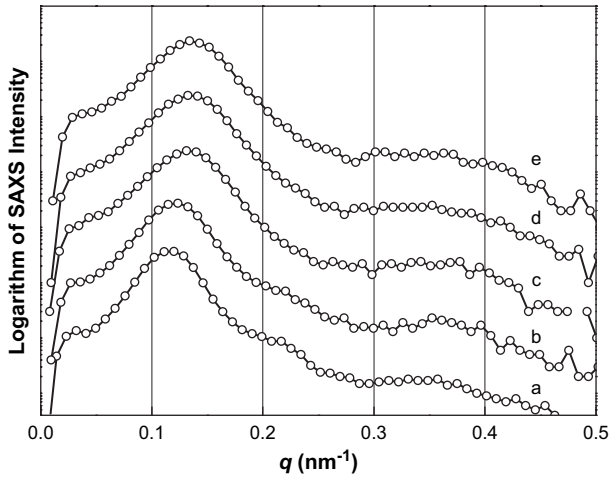

Fig. 4. One-dimensional equatorial scan data obtained from the two-dimensional SAXS patterns: (a) 0 s (unelongated); (b) 18 s ($\epsilon = 0.18$, $\lambda = 1.20$); (c) 77 s ($\epsilon = 0.77$, $\lambda = 2.16$); (d) 90 s ($\epsilon = 0.90$, $\lambda = 2.46$); (e) 110 s ($\epsilon = 1.10$, $\lambda = 3.00$).

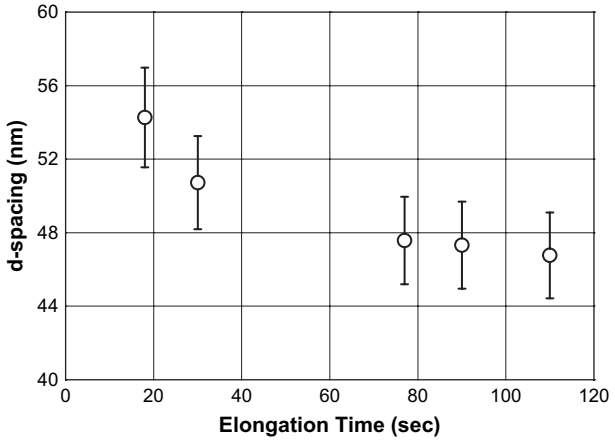

Fig. 5. The change in *d*-spacing of the *100* peak, measured during the case I elongation.

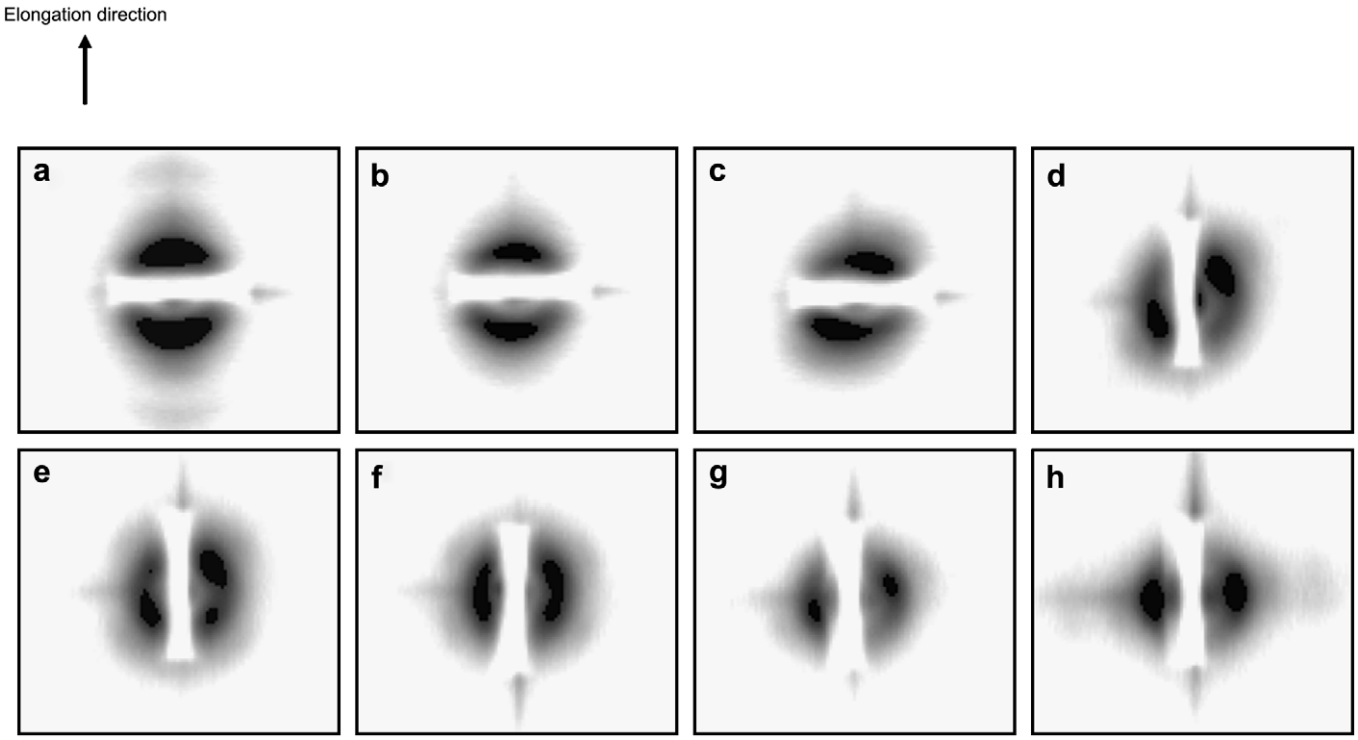

Fig. 6. Two-dimensional SAXS patterns of the unelongated and elongated samples collected during the case II elongation at (a) 0 s (unelongated), (b) 20 s ($\epsilon = 0.2$, $\lambda = 1.2$), (c) 40 s ($\epsilon = 0.4$, $\lambda = 1.5$), (d) 60 s ($\epsilon = 0.6$, $\lambda = 1.8$), (e) 70 s ($\epsilon = 0.7$, $\lambda = 2.0$), (f) 80 s ($\epsilon = 0.8$, $\lambda = 2.2$), (g) 100 s ($\epsilon = 1.0$, $\lambda = 2.7$) and (h) 180 s ($\epsilon = 1.8$, $\lambda = 6.1$).

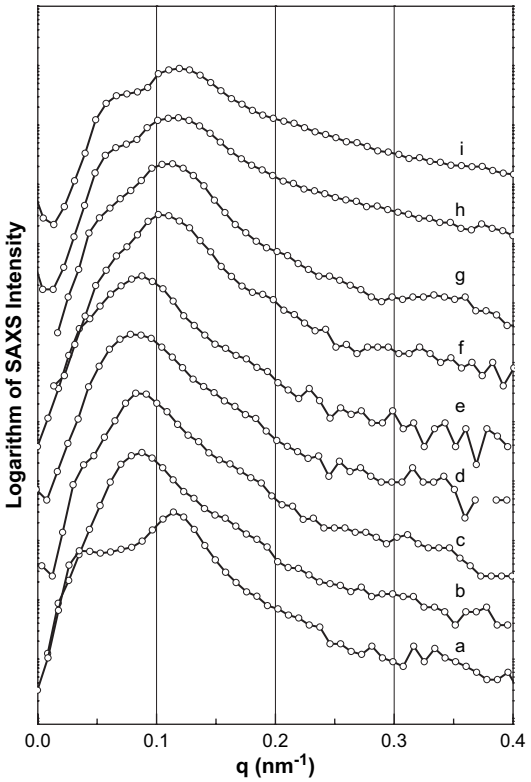

Fig. 7. One-dimensional scan data obtained on the two-dimensional SAXS patterns shown in Fig. 3: (a) 10 s ($\epsilon = 0.1$, $\lambda = 1.1$); (b) 40 s ($\epsilon = 0.4$, $\lambda = 1.5$); (c) 50 s ($\epsilon = 0.5$, $\lambda = 1.7$); (d) 60 s ($\epsilon = 0.6$, $\lambda = 1.8$); (e) 70 s ($\epsilon = 0.7$, $\lambda = 2.0$); (f) 90 s ($\epsilon = 0.9$, $\lambda = 2.5$); (g) 100 s ($\epsilon = 1.0$, $\lambda = 2.7$); (h) 150 s ($\epsilon = 1.5$, $\lambda = 4.5$); (i) 180 s ($\epsilon = 1.8$, $\lambda = 6.1$). The calculated positions of the high order peaks under the assumption of a lamellar ordering were marked as downward arrows.

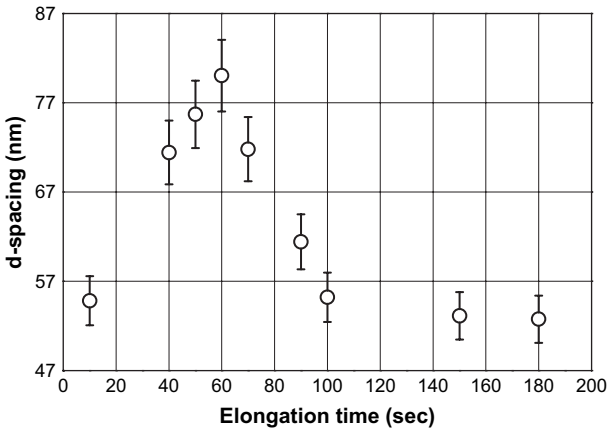

Fig. 8. The change in *d*-spacing of the *100* peak, measured during the case II elongation.

layer normal was mostly aligned along the stretching direction. During the continuous elongation, it gradually moved to the equator and appeared almost on the equator at 180 s. The inclination of the *100* peak indicates the inclination of the lamellar phase during the elongation.

In Fig. 7, we observed the intense *100* peak and additional X-ray intensities, whose q values were almost in the ratio 1:2:3. The existence of the meridional peak intensities of the initial sample revealed that the lamellar normals are aligned along the stretching direction. Based on the position of the most intense *100* reflection, the lamellar period, D, was estimated at various stages of elongation and is shown in Fig. 8. The data showed that the D was highly increased by approximately 20% in the middle of elongation [$40 \leq t$ (s) ≤ 70], and then slightly decreased to almost the initial value. A

large increase in the range $40 \leq t\,(s) \leq 70$ was due to the expansion of the lamellar period, driven by the elongation and deformation of the soft PEB domains. The following decrease on further elongation resulted mainly from the improved molecular and domain orientation to the stretching direction. A slight initial increase of the half width up to $\epsilon = 0.2$ was due to the deformation of the lamellar morphology, generated by the elongation and deformation of the soft PEP domains, together with the fragmentation of the grain structure of the SEP. Fig. 9(a)–(e) displays the data, scanned in the azimuthal direction (β) along the most intense *100* peaks in Fig. 6. In Fig. 9(a), the existence of the peak at $\beta = 90^\circ$ indicated that the orientation of the lamellar normal of the initial case II sample was almost aligned along the stretching direction (perpendicular lamellae). Fig. 9(b), for the sample collected at $\epsilon = 0.4$, shows that the main peak intensity was moved to the angle β of approximately 128°, indicating the slight rotation of the original, perpendicular lamellae to the stretching direction.

Fig. 9(c) shows the azimuthal scan data at $\epsilon = 0.7$. The peak width in the 2θ direction became broader, indicating the decrease of the grain size due to the deformation or distortion of the lamellar domains. The continuous elongation led to the fragmentation and realignment of the grain structure, coupled with the decreased packing order of the lamellae. In this figure, the main peak intensity was moved to the angle β of approximately 138°, indicating the slight movement of the original, perpendicular cylindrical domains to the stretching direction. Additional weak peak was also found at around 226°. The *100* peak was split to show the four-point pattern, typical of smectic-C type compounds. However, the intensities of both peaks along the azimuthal direction were not the same, indicating that the lamellar phase was still preferentially inclined to the stretching direction. The broadness and existence of two azimuthal peak intensities may be caused by the rotation of the grains that are preferentially aligned in two different directions. In Fig. 9(d) and (e), an additional weak peak was almost disappeared and the intense *100* peak was moved further to the equator. These figures show the *100* peak almost on the equator, indicating the rotation of the lamellar phase by approximately 90° to the stretching direction.

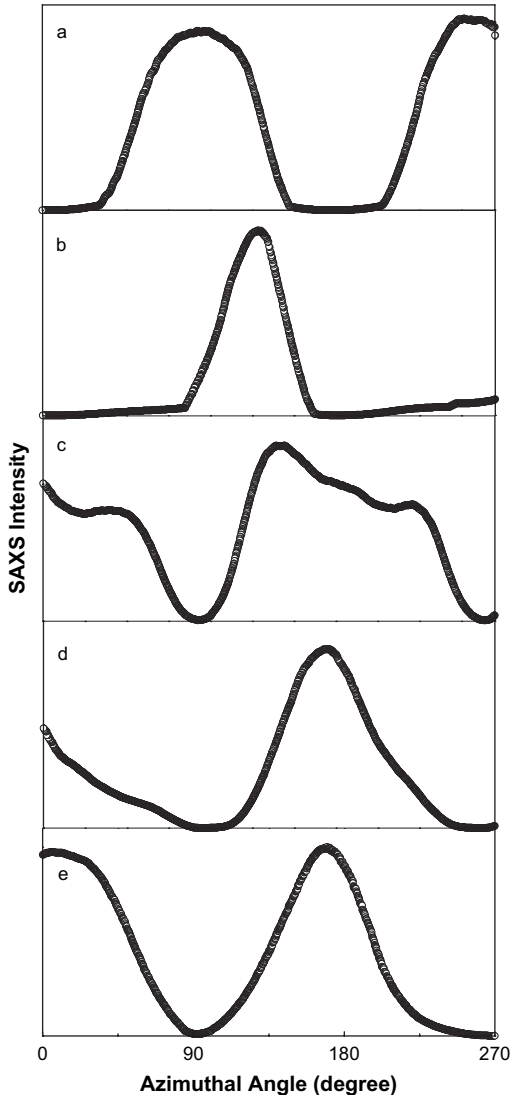

Fig. 9. The azimuthally scanned data along the strongest *100* peak in Fig. 6: (a) 10 s ($\epsilon = 0.1$, $\lambda = 1.1$); (b) 40 s ($\epsilon = 0.4$, $\lambda = 1.5$); (c) 70 s ($\epsilon = 0.7$, $\lambda = 2.0$); (d) 100 s ($\epsilon = 1.0$, $\lambda = 2.7$); (e) 180 s ($\epsilon = 1.8$, $\lambda = 6.1$).

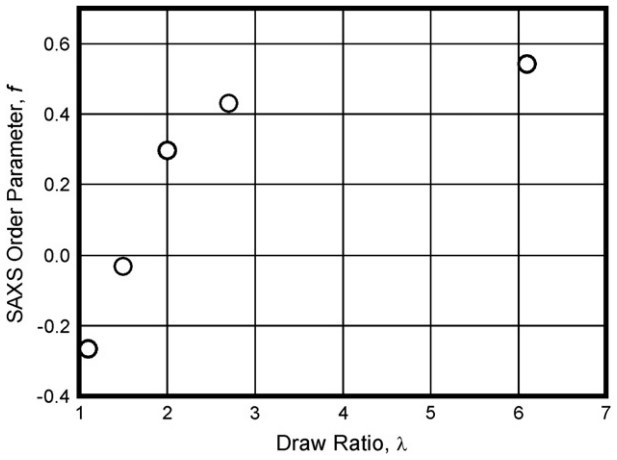

Fig. 10. Plot of order parameter, *f*, vs. Hencky strain determined from the azimuthal intensity distribution along the *100* peak in Fig. 9.

The degree of orientation of the lamellar domains can be quantitatively expressed by order parameter, *f*, defined by the following equation:

$$f \equiv \frac{3\langle \cos^2 \beta \rangle - 1}{2} = \frac{\int I(\beta)|\sin\beta|\left(\frac{3}{2}\cos^2\beta - \frac{1}{2}\right)\mathrm{d}\beta}{\int I(\beta)|\sin\beta|\mathrm{d}\beta} \tag{2}$$

where $\langle \cos^2 \beta \rangle$ is the mean-square cosine of the azimuthal angle and $I(\beta)$ is the azimuthal intensity distribution corresponding to the peak widening due to misorientation. Based on the azimuthal scan data along the first order peak shown in Fig. 9, the *f*s at different levels of Hencky strains were estimated by Eq. (2) and are plotted in Fig. 10. In Fig. 10, the measured values of *f* for the orientation of the lamellar domains increase rapidly as the elongation proceeds up to near $\lambda \approx 2$ ($\epsilon \approx 0.7$), indicating that the realignment or rearrangement process of the lamellar domains is significant in the early stage of elongation. Beyond $\lambda \approx 2$, it continues to increase, but less rapidly by further alignment of the lamellae into the stretching direction.

3.4. Morphological change at small deformation

The elongational flow-induced deformation behavior of both the perpendicular and parallel lamellar phases has been investigated at various stages of elongation. The data shown here pointed out that the morphological evolution of the lamellar phase of the case I and case II samples varied with the initial alignment of the lamellae to the stretching direction. Due to the different geometrical arrangements of the PS and PEP blocks, the small deformation of

both samples causes the preferential elongation of the PS, together with PEP (case I) or PEP (case II) chains, depending on their geometrical arrangement to the elongation direction. In our EFOR system, the plane-polarized light was set to pass through the specimen during elongation and the split intensities, *DP*, and *DS*, perpendicular and parallel to the stretch direction, respectively, were detected with silicon photoelectric detectors. The retardation, $R(t)$, provides information on the initial molecular orientation in the first stage of elongation. It can be expressed by the phase difference Δt between the polarized lights on the detectors, with intensities *DP* and DS:

$$R(t) = \frac{DS - DP}{DS + DP} = \sin[2\Delta(t)] \tag{3}$$

Experimentally, the phase difference Δt is determined by the apparent retardation $R_{app}(t)$ and measured intensities, DS_a ($DS + D_o$, where D_o is the unpolarized background) and DP_a ($DP + D_o$) and on the detectors:

$$R_{app}(t) = \frac{DS_a - DP_a}{DS_a + DP_a} = \frac{DS - DP}{DS + DP + 2D_o} = A_m \sin[2\Delta(t)] \tag{4}$$

where A_m [$=(DP + DS)/(DP + DS + 2D_o)$] denotes the amplitude factor. To eliminate the effect of the preexisting alignment of the lamellae in the unoriented specimens, the initial difference between the intensities DP_a and DS_a was offset in the beginning of each EFOR measurement. The $R_{app}(t)$ measured during the elongation of the PS melt started with the negative value, whereas the one from low-density polyethylene exhibited the positive values in the beginning of elongation [30,31].

Fig. 11(a) and (b) shows the apparent retardation data for the case I and case II samples. The data between the start up to approximately 5.5 s were not monitored due to the idle time of the EFOR equipment. In these data, the $R_{app}(t)$s of the case I and case II melts showed the negative and positive values during elongation until about 20 s. These data suggested that the elongational behavior of the case I and case II samples at small deformation up to near their yielding points ($\epsilon \sim 0.4$ and 0.2 for the case I and case II samples, respectively, shown in Fig. 1) was controlled by the preferential deformation of the PS (case I) or PEP (case II) domain. For the case I sample, the parallel lamellar morphology may not be much changed by the rigidity and parallel orientation of the PS domains. The gradual increase of its $\eta_E(\dot{\epsilon}_o; t)$ was probably due to the refinement of the molecular elongation of the PS and PEP chains, probably in the localized disordered regions. The elongation of the case II sample initially induced the deformation of the relatively soft PEP domains, which gave rise to the reorganization of the grain structure to the stretching direction.

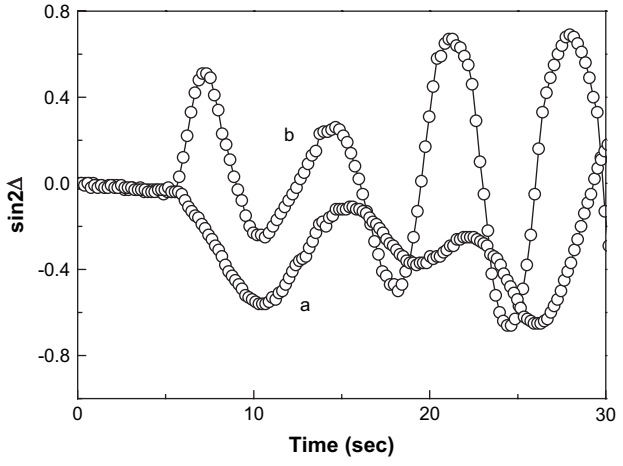

Fig. 11. Plots of apparent retardation $\sin[2\Delta(t)]$ vs. time measured during the (a) case I and (b) case II elongations.

3.5. Morphological change at large deformation

On further elongation beyond the yielding point of the case I sample, the elongational viscosity exhibited almost the steady state before rupture. The corresponding SAXS data of the samples collected at $\epsilon = 0.9$ showed almost the same features as those seen in the unelongated sample, indicating that the parallel lamellar alignment persisted up to its rupture. However, the packing order of the PS lamellae became slightly reduced due to the high degree of elongation along the stretching direction. The broadness of the peak at this stage of elongation also indicated that the domain and grain structure of the case I samples at $\epsilon = 0.9$ were deformed and fragmented. These results pointed out that the high degree of elongation of the case I sample caused the slight rearrangement of the grain structure to the stretching direction. The sharpness of the peak and decrease of the peak position in the SAXS data at $\epsilon = 2.16$ appeared due to the further elongation of the deformed lamellae to the stretching direction. The increased peak sharpness indicated the improved structural order of the highly elongated lamellar phase. The persistence of the similar characteristics shown in Fig. 3(a) through (e) also pointed out that the orientation of the initial lamellar morphology was almost maintained up to rupture.

In the middle of elongation ($0.2 < \epsilon \leq 0.7$), the $\eta_E(\dot{\epsilon}_o; t)$ of the case II sample was almost in the steady state. The SAXS data shown in Fig. 7(b) and (c) show that the lamellar domains of the case II samples were gradually rotated into the stretching direction. In the corresponding one-dimensional SAXS data in Fig. 6(b) and (c), the scattering vector q values of the peaks slightly moved to the small angle region, probably due to the increased structural imperfection by the large deformation. At $\epsilon = 0.7$ shown in Fig. 6(c), the lamellar domains were preferentially inclined to the stretching direction by approximately 30°. The absence of the four-point pattern, indicative of the absence of the "chevron" morphology [32], was probably due to the initial alignment of the domains which was not exactly perpendicular to the elongation direction and caused the domains to rotate in either one of the two possible directions. It was previously reported that the inclination of the cylinder phase was occurred due to the positional correlation of the matrix polymer chains which did not allow the rotation of the domains to be aligned to the stretching direction [16].

On further elongation beyond $\epsilon = 0.7$, the $\eta_E(\dot{\epsilon}_o; t)$ of the case II sample continued to increase further up to its rupture and displayed the strong strain-induced hardening behavior. Fig. 7(h) displays a series of equatorial X-ray peaks, confirming the rotation of the perpendicular lamellae into the parallel alignment. The parallel alignment of the lamellae was achieved at high temperature where the molecular association became weaker by the increased thermal motion of molecules than at low temperatures. The domains composed of the associated mobile molecules confined by their interfaces seem to rotate further to the stretching direction. A similar result was found during shearing of diblock copolymers, showing that a large amount of shear produced the parallel or perpendicular alignment of lamellar domains where the domain interfaces were aligned to the shearing direction [8–13].

4. Conclusions

The combination of the EFOR and SAXS measurements provided the information on the structural evolution of the lamellar domains under elongation. The deformation behavior varied with the initial alignment of the lamellar domains. The elongation of the case I sample induced the preferential elongation of the relatively rigid PS domains in the beginning of elongation and the initial parallel morphology was almost persisted at large deformation up to rupture. The reorganization of the domain structure, along with yielding of the PS domains, decreased the $\eta_E(\dot{\epsilon}_o; t)$ beyond the yielding

point of the case I sample. For the case II sample, the initial elongation induced the elongation of the soft PEP matrix. The continuous elongation of the case II sample deformed and rotated the initial grain structure to the stretching direction. The deformation of the domain structure decreased the $\eta_E(\dot{\epsilon}_o; t)$ values in the range $0.2 < \epsilon \leq 0.7$, but the further orientation of the molecules and lamellae at high degree of elongation highly increased the $\eta_E(\dot{\epsilon}_o; t)$ and exhibited the prominent strain-induced hardening behavior. The changes of $\eta_E(\dot{\epsilon}_o; t)$s of the case I and case II samples were mostly governed by the morphological evolution of the lamellar domain and grain structures of both samples.

Acknowledgements

This work was supported by the Korea Research Foundation Grant funded by the Korean Government (MOEHRD, Basic Research Promotion Fund) (KRF-2007-D00141).

References

[1] Hamley IW. The physics of block copolymers. New York: Oxford University Press; 1998.
[2] Winey KI, Patel SS, Larson RG, Watanabe H. Macromolecules 1993;26:2542.
[3] Polis DL, Winey KI. Macromolecules 1998;31:3617.
[4] Okamoto S, Saijo K, Hasimoto T. Macromolecules 1994;27:5547.
[5] Zhang Y, Wiesner U, Spiess HW. Macromolecules 1995;28:778.
[6] Gupta VK, Krishnamoorti R, Chen ZR, Kornfield JA. Macromolecules 1996;29:875.
[7] Gupta VK, Krishnamoorti R, Chen ZR, Kornfield JA, Smith SD. Macromolecules 1996;29:1359.
[8] Chen ZR, Issaian AM, Kornfield JA, Smith SD, Grothaus JT, Satkowski MM. Macromolecules 1997;30:7096.
[9] Oelschlaeger C, Gutmann JS, Wolkenhauer M, Spiess HW, Knoll K, Wilhelm M. Macromol Chem Phys 2007;208(16):1719.
[10] Leist H, Geiger K, Wiesner U. Macromolecules 1999;32:1315.
[11] Wiesner U. Macromol Chem Phys 1997;198:3319.
[12] Pinheiro BS, Winey KI. Macromolecules 1998;31:4447.
[13] Takahashi T, Toda H, Minagawa K, Takimoto JI, Iwakura K, Koyama K. J Appl Polym Sci 1995;56:411.
[14] Fujumura M, Hashimoto T, Kawai H. Rubber Chem Technol 1978;51:215.
[15] Kawai H, Hashimoto T. J Macromol Sci 1980;B17:427.
[16] Seguela R, Prudhomme J. Macromolecules 1981;14:197.
[17] Pakula T, Saijo K, Kawai H, Hashimoto T. Macromolecules 1985;18:7096.
[18] Yamaoka I, Kimura M. Polymer 1993;34:4399.
[19] Cohen Y, Albalak RJ, Dair BJ, Capel MS, Thomas EL. Macromolecules 2000;33:6502.
[20] Kotaka T, Kojima A, Okamoto M. Rheol Acta 1997;36:646.
[21] Okamoto M, Kojima A, Kotaka T. Polymer 1997;39:2149.
[22] Kano Y, Okamoto M, Kotaka T. Polymer 1999;40:2459.
[23] Kim YH, Okamoto M, Kotaka T, Ougizawa T, Tchiba T, Inoue T. Polymer 2000;41:4747.
[24] Kotaka T, Okamoto M, Kojima A, Kwon YK, Nojima S. Polymer 2001;42:1207.
[25] Kotaka T, Okamoto M, Kojima A, Kwon YK, Nojima S. Polymer 2001;42:3223.
[26] Kobori Y, Kwon YK, Okamoto M, Kotaka T. Macromolecules 2003;36:1656.
[27] Meissner J, Hostettler J. Rheol Acta 1994;33:1.
[28] Rudd JF. In: Brandrup J, Immergut EH, editors. Polymer handbook. 3rd ed. New York: John Wiley & Sons; 1989.
[29] Gubler X, Kovacs X. J Polym Sci 1959;34:551.
[30] Janeschitz-Kriegel H. Polymer melt rheology and flow birefringence. Berlin: Springer-Verlag; 1983.
[31] White JL. Principles of polymeric engineering rheology. New York: Wiley; 1990.
[32] Honeker CC, Thomas EL. Chem Mater 1996;8:1702.